

# Finding the Maximum Independent Sets of Platonic Graphs Using Rydberg Atoms

Andrew Byun<sup>ID</sup>,<sup>†</sup> Minhyuk Kim<sup>ID</sup>,<sup>†</sup> and Jaewook Ahn<sup>ID</sup><sup>\*</sup>

Department of Physics, Korea Advanced Institute of Science and Technology (KAIST), Daejeon 34141, Korea



(Received 2 March 2022; revised 25 May 2022; accepted 21 June 2022; published 8 July 2022)

We present Rydberg-atom-array experiments performed to find the maximum independent sets of Platonic graphs. Three Platonic graphs—the tetrahedron, cube, and octahedron of Platonic solids—are constructed with atoms and Rydberg interatomic interactions, representing, respectively, the vertices and edges of the graphs. In particular, the three-dimensional Platonic graph structures are transformed onto the two-dimensional plane by using Rydberg quantum wires that couple otherwise uncoupled long-distance atoms. The maximum independent sets of the graphs correspond to the antiferrolike many-body ground-state spin configurations of the as-constructed Rydberg-atom arrays, which are successfully probed by quasiadiabatic control of the Rydberg-atom arrays from the paramagnetic phase to their antiferrolike phases. Our small-scale quantum simulations using fewer than 18 atoms are limited by experimental imperfections, which can be easily improved upon by the state-of-the-art Rydberg-atom technologies for scales of more than 1000 atoms. Our quantum-wire approach is expected to pave a new route toward large-scale quantum simulations.

DOI: 10.1103/PRXQuantum.3.030305

## I. INTRODUCTION

Breakthroughs in artificial quantum many-body systems have brought unforeseen opportunities to explore problems in physics, chemistry, materials science, and medicine [1–5]. In recent years, Rydberg-atom systems in particular have advanced rapidly, demonstrating quantum-mechanical simulations of the nature of complex quantum materials [6–10]. There are many advantages to using Rydberg atoms in quantum simulations. Interactions of Rydberg atoms are strong and short-ranged enough to feature the mesoscopic nature of lattice Hamiltonians such as Ising, XY, and XXZ models [11–15]. Rydberg-atom arrays are easily scalable [16–18] to generate entanglements of a huge number of atoms [19], to investigate many-body dynamics near quantum phase transitions [20–24], and to study topological effects [25]. Three-dimensional (3D) arrangements [26,27] of Rydberg atoms are used to probe the physical properties of tree lattices [28] and are expected to investigate the many-body physics of more complex

arrangements [27]. In recent reports [29,30], the number of Rydberg atoms has started to exceed a few hundred, boosting the motivation toward computational advantages in solving combinatorial optimization problems [31–34]. This approach mainly uses adiabatic evolution [35]: a system is forced to remain in the ground state of instantaneous Hamiltonians changing in time and then finally evolved to solutions of a classical problem Hamiltonian. Although the result is not deterministic compared to classical heuristic approaches, it is expected to give computational advantages, as it can deal with a few states out of a  $2^N$  basis for  $N$  atoms.

Rydberg-atom technology uses neutral atoms captured and arranged by focused optical beams and coupled with each other through Rydberg-atom dipole-blockade interactions [6]. The interatomic distances of coupled Rydberg atoms are lower and upper bounded by the Rayleigh range and Rydberg-blockade distance, respectively, which strongly limits the geometries and topologies of the qubit couplings of a Rydberg-atom array [27]. So, when Rydberg-atom arrays are used in combinatorics—as, e.g., in this paper, to find the maximum independent set (MIS) of a given graph [31,33,34]—one limitation is the gap between the distance-dependent atom interactions and the distance-independent graph edges. One of the latest Rydberg-atom technologies to overcome such a limit is quantum wiring [36], the use of auxiliary atoms to couple remote atoms, which enables otherwise impossible complex such as nonplanar and high-degree graphs [33]. The

\*jwahn@kaist.ac.kr

<sup>†</sup>These two authors contributed equally.

Published by the American Physical Society under the terms of the [Creative Commons Attribution 4.0 International license](#). Further distribution of this work must maintain attribution to the author(s) and the published article's title, journal citation, and DOI.

other limitation is the technical barrier to arranging the focused optical beams in 3D space [12].

In this paper, we use quantum wires to demonstrate topology-preserving transformations of a Rydberg-atom system from a 3D surface to a plane. Three Platonic graphs—the tetrahedron, cube, and octahedron graphs—are experimentally implemented and their many-body ground states, which are the MISs of the Platonic graphs, are probed via quantum adiabatic controls [20,35].

The rest of the paper is organized as follows. The model Hamiltonian of Rydberg-atom arrays is defined in Sec. II along with the various usages of the quantum wires in our experiments. We then describe the phase diagrams of the Rydberg-atom arrays for the Platonic graphs in Sec. III and the experimental procedure in Sec. IV. The resulting quantum simulation data of the Platonic graphs are reported in Sec. V. We conclude by discussing the scaling issues and outlooks in Sec. VI.

## II. QUANTUM WIRES FOR PLATONIC GRAPHS

We consider a mathematical graph,  $G(V, E)$ , to model the interactions of an atom array, in which the vertices,  $V$ , and edges,  $E$ , respectively, represent the atoms and pairwise atom-atom interactions. In the Rydberg-atom-blockade regime [6] of adjacent atoms, the Hamiltonian

$\hat{H}_G$  of the atom array in  $G$  is given by

$$\hat{H}_G = \frac{\hbar}{2} \sum_{i \in V} (\Omega \hat{\sigma}_{x,i} - \Delta \hat{\sigma}_{z,i}) + \sum_{(i,j) \in E} U \hat{n}_i \hat{n}_j, \quad (1)$$

where  $\Omega$  and  $\Delta$  are the Rabi frequency and detuning of the optical excitation of the atoms from the ground state, denoted by  $| \downarrow \rangle = | 0 \rangle$ , to a Rydberg state,  $| \uparrow \rangle = | 1 \rangle$ , and  $U = C_6/d^6$  is the van der Waals interaction, with coefficient  $C_6$ , between the adjacent atoms. The distance of all adjacent atom pairs is maintained at  $d$ , which is smaller than the blockade distance,  $d_R = (C_6/\hbar\Omega)^{1/6}$ , i.e.,  $d < d_R$ .  $\hat{\sigma}_{x,z}$  and  $\hat{n} = (\hat{\sigma}_z + 1)/2$  are the operators for Pauli  $x$  and  $z$  and the Rydberg excitation number. This Hamiltonian for quantum Ising spins [20,21] has been considered for MIS problems of  $G$  [31–34].

Figure 1 shows, in the first row, the three Platonic graphs to be constructed in this work. They are, in graph-theory notation,  $K_4$ , the tetrahedron graph ( $f = 4$ ),  $Q_3$ , the cube graph ( $f = 6$ ), and  $K_{2,2,2}$ , the octahedron graph ( $f = 8$ ), as shown in Figs. 1(a)–1(c), respectively, where  $f$  denotes the facet number, i.e.,  $f = 2 - ||V|| + ||E||$  in Euler's polyhedron formula. While the given Platonic solids are three-dimensional, their graphs are planar, so they are in principle implementable on the plane. However, planar arrangements of atoms for these planar graphs require non-adjacent atoms to be coupled as if they were adjacent, so we choose to use quantum wires [33].

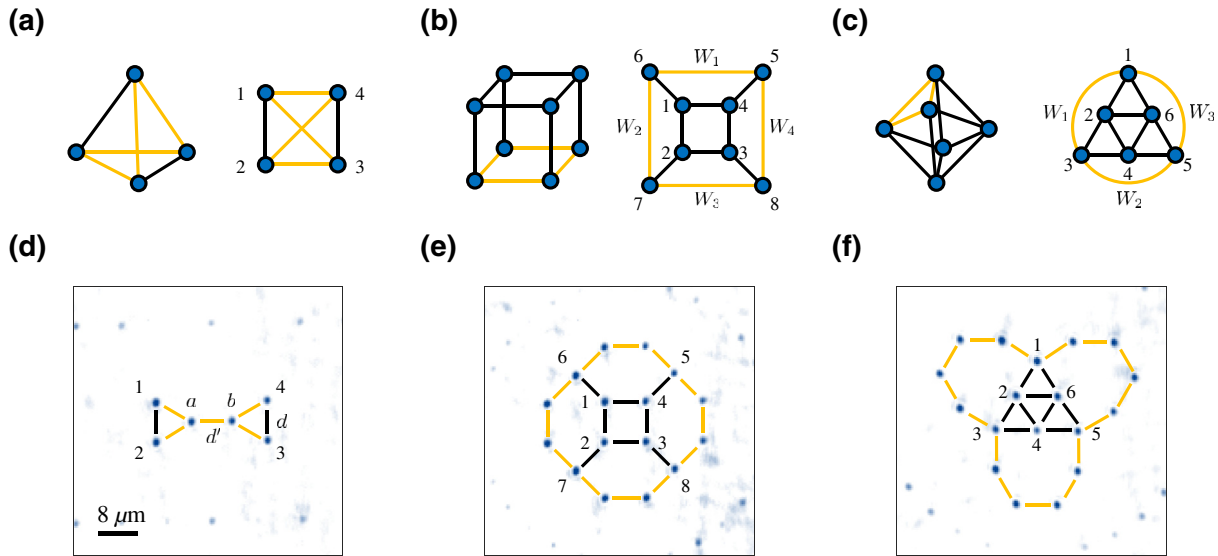


FIG. 1. The Platonic graphs and their two-dimensional (2D) arrangements. (a)–(c) The tetrahedral graph  $K_4$  (a), the cube graph  $Q_3$  (b), and the octahedron graph  $K_{2,2,2}$  (c), in which the yellow edges are to be replaced by quantum wires. (d) The quantum-wired tetrahedral graph,  $K'_4$ , uses one quantum wire,  $W$ , of two wire atoms, to replace the four yellow edges of  $K_4$ , so there are six atoms and seven equal-length edges in  $K'_4$ . (e) The quantum-wired cube graph,  $Q'_3$ , uses four quantum wires,  $W_{1,2,3,4}$ , each made up of two wire atoms, to replace the four yellow edges of  $Q_3$ , so there are 16 atoms and 20 edges in  $Q'_3$ . (f) The quantum-wired octahedron graph,  $K'_{2,2,2}$  uses three quantum wires,  $W_{1,2,3}$ , each made up of four wire atoms, to replace the three yellow edges of  $K_{2,2,2}$ , so there are 18 atoms and 24 edges in  $K'_{2,2,2}$ . The lengths are  $d'$  for the edges involved with quantum wires and  $d$  for all other edges.

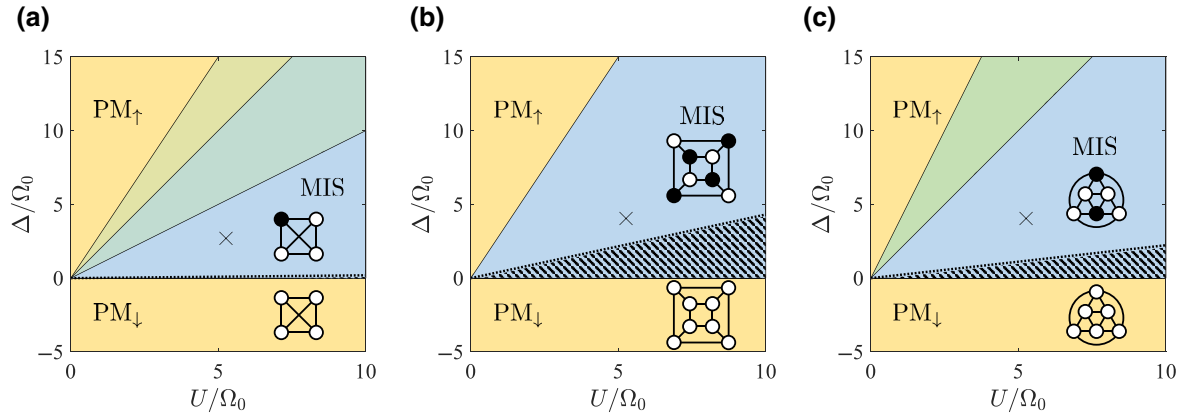


FIG. 2. The phase diagrams of the Platonic graphs: (a) the tetrahedron graph  $K_4$ , (b) the cube graph  $Q_3$ , and (c) the octahedron graph  $K_{2,2,2}$ . There are two paramagnetic phases,  $PM_\downarrow$  and  $PM_\uparrow$  in the regions  $\Delta < 0$  and  $\Delta > 4U$ , respectively, and graph-dependent AF-like phases between them. The phase boundaries change due to neglected long-range interactions in Eq. (1); in particular, the  $\Delta = 0$  phase boundary shifts up to encompass the shaded areas in (a)–(c). The first AF-like phases above  $PM_\downarrow$  are the MIS phases (in blue) of the graphs, in which all adjacent atoms that are denoted by the edges of the graphs are Rydberg blockaded. (a) The MIS phase of  $K_4$  allows one Rydberg atom, i.e., the ground many-body state is the superposition of four singly excited configurations in Eq. (2). The other AF-like phases of  $K_4$  are the superpositions of doubly excited and triply excited configurations, located, respectively, at  $U < \Delta < 2U$  and  $2U < \Delta < 3U$ . (b) The MIS phase of  $Q_3$  is the superposition of two quadruply excited configurations as in Eq. (5). (c) The MIS phase of  $K_{2,2,2}$  is the superposition of three doubly excited configurations, as in Eq. (6), and the other AF-like phase is the superposition of three quadruply excited configurations, located in  $2U < \Delta < 4U$ . The experiments in Sec. V are performed by adiabatically evolving the atom arrays from the  $PM_\downarrow$  phase (at  $\Delta/\Omega_0 = -4.05$ ) to the MIS phases (at the cross-marked points,  $\Delta/\Omega_0 = 2.79$  for  $K_4$  and 4.05 for  $Q_3$  and  $K_{2,2,2}$ ).

Quantum wires [33,36] can be substituted for chosen edges of a graph  $G$ , either to replicate the Hamiltonian,  $H_G$ , by using local addressing fields, or to determine only the ground-state spin configurations of  $H_G$ , through non-local addressing fields and postselective compilations. As the former is experimentally daunting given current technologies, we use the latter version of quantum wires with no local addressing in this paper. For the MIS phase, which is defined by the parameter conditions,  $\Omega = 0$  and  $0 < \Delta < U$ , in Eq. (1), the edge of  $G$  can be replaced by a quantum wire, which is simply a chain of an even number of wire atoms in an antiferromagnetic (AF) spin state. In the MIS phase, in which no adjacent atoms are simultaneously excited to the Rydberg state, the state of the quantum wire—say, one with two atoms—must be in either  $|00\rangle_W$ ,  $|01\rangle_W$ , or  $|10\rangle_W$ , so the quantum wire introduces no additional energy [33].

As an example, let us consider the ground-state spin configurations of the tetrahedron graph,  $K_4$ , and compare them with those of a quantum-wired graph,  $K'_4$ . As shown in Fig. 1(d), our choice of  $K'_4$  has two wire atoms,  $a, b$ , which are used to couple the four atoms, 1, 2, 3, and 4, of  $K_4$ . The MIS ground state of the tetrahedron graph,  $K_4$ , is given by

$$|M(K_4)\rangle = \frac{|1000\rangle + |0100\rangle + |0010\rangle + |0001\rangle}{2}, \quad (2)$$

which is the four-qubit  $W$  state. The MIS ground state of the quantum-wired graph,  $K'_4$ , is given by

$$\begin{aligned} |M(K'_4)\rangle = & \sqrt{\frac{3}{32}}|10\rangle_W \otimes (|0001\rangle + |0010\rangle) \\ & + \sqrt{\frac{3}{32}}|01\rangle_W \otimes (|0100\rangle \\ & + |1000\rangle) + \sqrt{\frac{5}{32}}|00\rangle_W \otimes (|0101\rangle \\ & + |0110\rangle + |1001\rangle + |1010\rangle), \end{aligned} \quad (3)$$

where the first two terms satisfy the AF condition of the quantum wire but the last term fails. Therefore, if we simply discard the last term, by performing a conditional measurement of  $|M(K'_4)\rangle$ , given the condition of the AF configurations of the quantum wire, i.e.,  $|10\rangle_W$  and  $|01\rangle_W$  only, we can obtain the probability distribution of  $|M(K_4)\rangle$ . Using the *a priori* information about the symmetric phase relation of the graph, we obtain  $(|01\rangle_W + |10\rangle_W)|M(K'_4)\rangle \rightarrow |M(K_4)\rangle$ .

In general, the MIS ground states of a general graph  $G$  and its quantum-wired graph  $G'$  are related as follows:

$$\langle \text{AF}_W | M(G') \rangle \rightarrow |M(G)\rangle, \quad (4)$$

where  $|\text{AF}\rangle_W$  denotes the AF configurations of the quantum wire. In the experiments that follow, we use quantum-wired graphs,  $K'_4$  of one quantum wire,  $Q'_3$  of four quantum

wires, and  $K'_{2,2,2}$  of three quantum wires, as shown in Figs. 1(d)–1(f), respectively, to obtain the MIS ground states of the Platonic graphs  $K_4$ ,  $Q_3$ , and  $K_{2,2,2}$ .

### III. PHASE DIAGRAMS

The phase diagrams, or the ground-state spin configurations, of the Hamiltonian  $H_G(U, \Delta, \Omega = 0)$  are shown in Fig. 2 for the chosen Platonic graphs. The Hamiltonian  $H_G$  in Eq. (1) has two competing energy terms: the laser detuning term, which favors Rydberg atoms or up spins, and the interaction term, which favors nonadjacent double excitations. So, there are two paramagnetic phases,  $\text{PM}_\downarrow$  in the  $\Delta < 0$  region and  $\text{PM}_\uparrow$  in  $\Delta > 4U$ , with AF-like phases between them. Among the AF-like phases, we are interested in the MIS phase, which has no adjacent spin pairs at all. The MIS-phase regions differ by graph. Below, we consider the MIS phases of the tetrahedron, cube, and octahedron graphs, respectively.

#### A. Tetrahedron

The tetrahedron graph,  $K_4$ , has four vertices and each vertex has an edge with all others. In the MIS phase of no adjacent Rydberg atoms, only one atom is allowed to be excited to the Rydberg state, so the MIS ground state is  $|M(K_4)\rangle$  in Eq. (2), which is the superatom [37] superposition state. The MIS-phase region,  $M(K_4)$ , is located in  $0 < \Delta < U$ , as shown in Fig. 2(a). Between  $M(K_4)$  and  $\text{PM}_\uparrow$ , there are two additional AF-like phases in the regions  $U < \Delta < 2U$  and  $2U < \Delta < 3U$ , which have one and two adjacent Rydberg-atom pairs, respectively.

#### B. Cube

The cube graph,  $Q_3$ , has eight vertices, each of which has an edge with three other vertices. In the MIS phase,  $M(Q_3)$ , when one atom is in the Rydberg state, its three face-diagonal vertices are allowed to become Rydberg atoms, so the MIS ground state is

$$|M(Q_3)\rangle = \frac{|01010101\rangle + |10101010\rangle}{\sqrt{2}}. \quad (5)$$

Any other states, having fewer or more Rydberg atoms, are not ground states in any region in  $0 < \Delta < 3U$ , because Rydberg deexcitation or excitation of  $|M(Q_3)\rangle$  increases the energy by  $\Delta > 0$  or  $3U - \Delta$ , respectively. So, the MIS phase is the only AF-like phase of the cube graph, as shown in Fig. 2(b).

#### C. Octahedron

The octahedron graph,  $K_{2,2,2}$ , has six vertices, each of which has an edge with four other vertices. There are two

AF-like phases, the MIS phase of two Rydberg atoms, i.e.,

$$|M(K_{2,2,2})\rangle = \frac{|100100\rangle + |010010\rangle + |001001\rangle}{\sqrt{3}}, \quad (6)$$

and its inversion of four Rydberg atoms. Their equal-energy boundary is  $\Delta = 2U$ , so the MIS phase of the octahedron graph is located in  $0 < \Delta < 2U$  and the inverted MIS phase is in  $2U < \Delta < 4U$ , as shown in Fig. 2(c).

### IV. EXPERIMENTAL PROCEDURE

The MIS phases of the Platonic graphs,  $K_4$ ,  $Q_3$ , and  $K_{2,2,2}$ , are probed with quantum adiabatic control of Hamiltonians,  $H'_G$ , of the quantum-wired graphs,  $G' = K'_4$ ,  $Q'_3$ , and  $K'_{2,2,2}$ . The Hamiltonians are changed from their paramagnetic phase region,  $\text{PM}_\downarrow$ , to the MIS-phase region, respectively. Quantum simulation experiments of this kind have previously been performed with various Rydberg-atom arrays [12,21,28,29,33].

We use rubidium ( $^{87}\text{Rb}$ ) atoms, which are cooled in a magneto-optical trap and optically pumped to the ground state  $|0\rangle = |\downarrow\rangle = |5S_{1/2}, F = 2, m_F = 2\rangle$ . The atoms are then captured by far-off resonance dipole traps (optical tweezers) and arranged into positions for  $G'$  [9]. Table I lists the atom positions used in our experiments for  $G' = K'_4$ ,  $Q'_3$ , and  $K'_{2,2,2}$ . The nearest-neighbor distances are the same,  $d = 8.0 \pm 0.3 \mu\text{m}$ , and the blockade distance is  $d_R = 10.55 \mu\text{m}$  at  $\Omega_0 = 0.74 (2\pi)\text{MHz}$ . The Rydberg state,  $|1\rangle = |\uparrow\rangle = |71S_{1/2}, J = 1/2, m_J = 1/2\rangle$ , is excited by the two-photon off-resonant transition,  $|0\rangle \rightarrow |m\rangle \rightarrow |1\rangle$ , via the intermediate state  $|m\rangle = |5P_{3/2}, F' = 3, m_{F'} = 3\rangle$ , detuned by  $\Delta_m = 560 (2\pi)\text{MHz}$ . We use a 780-nm laser field (a homemade external-cavity diode laser) of  $\Omega_{780} = 112 (2\pi)\text{MHz}$  for the  $|0\rangle \rightarrow |m\rangle$  transition and a 480-nm laser field (Toptica TA-SHG Pro) of  $\Omega_{480} = 7.4 (2\pi)\text{MHz}$  for  $|m\rangle \rightarrow |1\rangle$ . The two-photon effective Rabi frequency  $\Omega$  is varied up to the maximum  $\Omega_0 = \Omega_{780}\Omega_{480}/2\Delta_m = 0.74 (2\pi)\text{MHz}$ .

The atoms are initially in the  $\text{PM}_\downarrow$  phase, i.e.,  $|\Psi(t=0)\rangle = |0\rangle^{N'}$ , where  $N'$  the number of atoms in  $G'$ , and then they are adiabatically driven to their MIS phase,  $|\Psi(t=t_f)\rangle = |M(G')\rangle$ . The control parameters of  $H_{G'}$  in Eq. (1) are changed in three stages. In the first stage, the Rabi frequency  $\Omega(t)$  is linearly tuned on from  $\Omega(t=0) = 0$  to  $\Omega(t_1) = \Omega_0$  and the detuning  $\Delta(t)$  (the two-photon detuning between the ground and Rydberg state) is maintained at  $\Delta(t=0-t_1) = -3 \text{ MHz}$ . In the second stage, we maintain the Rabi frequency  $\Omega(t=t_1-t_2) = \Omega_0$  and linearly change the detuning to  $\Delta(t_2) = \Delta_f$ . In the final stage, the Rabi frequency is linearly changed to zero, i.e.,  $\Omega(t_f) = 0$ , and the detuning is maintained at  $\Delta(t=t_2-t_f) = \Delta_f$ . We use  $t_f = 4.0 \mu\text{s}$ ,  $t_1 = t_f/10$ ,  $t_2 = t_f - t_1$ , and  $\Delta_f = 2.0 \text{ MHz}$  for the tetrahedron experiment and 3.0

TABLE I. The atom positions for the experimental graphs.

Graph	Atom positions ( $x, y$ ) ( $\mu\text{m}$ )			
Tetrahedron, $K'_4$	1:	(−10.9, 4.0)	2:	(−10.9, −4.0)
	3:	(10.9, −4.0)	4:	(10.9, 4.0)
	$W:$	( $\pm 4.0, 0.0$ )		
Cube, $Q'_3$	1:	(−4.0, 4.0)	2:	(−4.0, −4.0)
	3:	(4.0, −4.0)	4:	(4.0, 4.0)
	5:	(9.7, 9.7)	6:	(−9.7, 9.7)
	7:	(−9.7, −9.7)	8:	(9.7, −9.7)
	$W_1:$	( $\pm 4.0, 15.3$ )	$W_2:$	(−15.3, $\pm 4.0$ )
	$W_3:$	( $\pm 4.0, −15.3$ )	$W_4:$	(15.3, $\pm 4.0$ )
	1:	(0.0, 9.8)	2:	(−4.0, 2.9)
Octahedron, $K'_{2,2,2}$	3:	(−8.0, −4.0)	4:	(0.0, −4.0)
	5:	(8.0, −4.0)	6:	(4.0, 2.9)
	$W_1:$	(−6.9, 13.8) (−18.9, 6.9)	(−14.9, 13.8) (−14.9, 0.0)	
	$W_2:$	(−8.0, −12.0) (4.0, −18.9)	(−4.0, −18.9) (8.0, −12.0)	
	$W_3:$	(14.9, 0.0) (14.9, 13.8)	(18.9, 6.9) (6.9, 13.8)	

MHz for the cube and octahedron experiments.  $\Omega(t)$  and  $\Delta(t)$  are changed with a radio-frequency programmable synthesizer (Moglabs XRF) and acousto-optic modulators (AOMs) [28]. The final Hamiltonian parameters are set to  $(U/\Omega_0, \Delta_f/\Omega_0) = (5.27, 2.70)$  for the tetrahedron  $K_4$ , and  $(5.27, 4.05)$  for the cube  $Q_3$  and octahedron  $K_{2,2,2}$  experiments, which are located in their respective MIS phases as in Fig. 2.

After the atoms are driven to the MIS phase, their final states are measured by collecting the fluorescence images of the cyclic transition,  $|5S_{1/2}, F=2\rangle \leftrightarrow |5P_{3/2}, F'=3\rangle$ , in an electron-multiplying charge-coupled device (Andor iXon Ultra 897). The atoms in  $|0\rangle$  remain in the dipole traps and emit the fluorescence, while the atoms in  $|1\rangle$  are pushed away from the dipole traps, emitting no fluorescence. There are false-measurement errors, the false positive,  $P_{0 \rightarrow 1} = 0.12$ , and false negative,  $P_{1 \rightarrow 0} = 0.09$ , and bit-flip errors, which are mainly due to the single-atom trap loss due to the finite temperature and imperfect optical pumping, respectively [12,28]. We repeat the above measurement procedure 927 times for  $K_4$ , 3292 times for  $Q_3$ , and 1574 times for  $K_{2,2,2}$  to obtain their probability distributions of all spin configurations.

## V. RESULTS

Before performing the quantum simulation of the Platonic graphs, we first test the working principle of the quantum wires by using an example of  $K'_4$  and varying the edge distance of the quantum-wired graph. We use two kinds of edges,  $d_{12} = d_{34} = d = 0.76d_R$  and  $d_{1a} = d_{2a} = d_{ab} = d_{b3} = d_{b4} = d'$ , which are black- and yellow-colored edges, respectively, in Fig. 1(d), where  $a$  and  $b$  denote the two wire atoms and  $d'$  is the length of the edges

involved with the wire atoms. We use six different atom arrays of  $d'$  varying from  $0.8d = 0.61d_R$  to  $1.3d = 0.99d_R$  as in Fig. 3(a) (from left to right). Note that, as  $d'/d$  increases from zero to  $\infty$ , the six-atom system changes from a superatom to a pair of isolated dimers and the  $d' = d$  case corresponds to the  $K'_4$  graph in the third column in Fig. 3.

In Fig. 3(b), we show configuration-dependent fluorescence images of the atoms adiabatically driven to the MIS-phase condition, i.e.,  $0 < \Delta_f/U = 0.51 < 1$ . There are five characteristic spin configurations, which are, from top to bottom,  $|00\rangle_W|1010\rangle$ ,  $|00\rangle_W|1001\rangle$ ,  $|01\rangle_W|1000\rangle$ ,  $|11\rangle_W|1010\rangle$ , and  $|11\rangle_W|1001\rangle$ . Other spin configurations of the same rotational or reflection symmetries are observed similarly. The contrasts of the images in Fig. 3(b) are normalized per column to compare their relative occurrences among the spin configurations and graphs. In the first column, for  $d'/d = 0.8$ , the most strongly interacting six atoms, the most frequently observed configuration is  $|00\rangle_W|1010\rangle$ , which has both of the wire atoms in the ground state. In the last column, for  $d'/d = 1.3$ , the pair of isolated dimers,  $|11\rangle_W|1001\rangle$  is the most frequently observed configuration, in which both the wire atoms are Rydberg atoms. Both of these cases,  $|00\rangle_W|1010\rangle$  and  $|11\rangle_W|1001\rangle$ , fail the AF quantum-wire condition. On the other hand, in the third column, which corresponds to  $K'_4$  ( $d' = d$ ), it is significant that the highlighted  $|01\rangle_W|1000\rangle$  configuration is observed, which satisfies the AF quantum-wire condition. The other two significant observed configurations are  $|00\rangle_W|1010\rangle$  and  $|00\rangle_W|1001\rangle$ , which agree well with the expected ground many-body state of  $K'_4$  in Eq. (3). Therefore, the desired graph,  $G' = K'_4$ , is adequately implemented with the condition of atom distances,  $d' = d = 0.76d_R$ , and the same condition is used, after

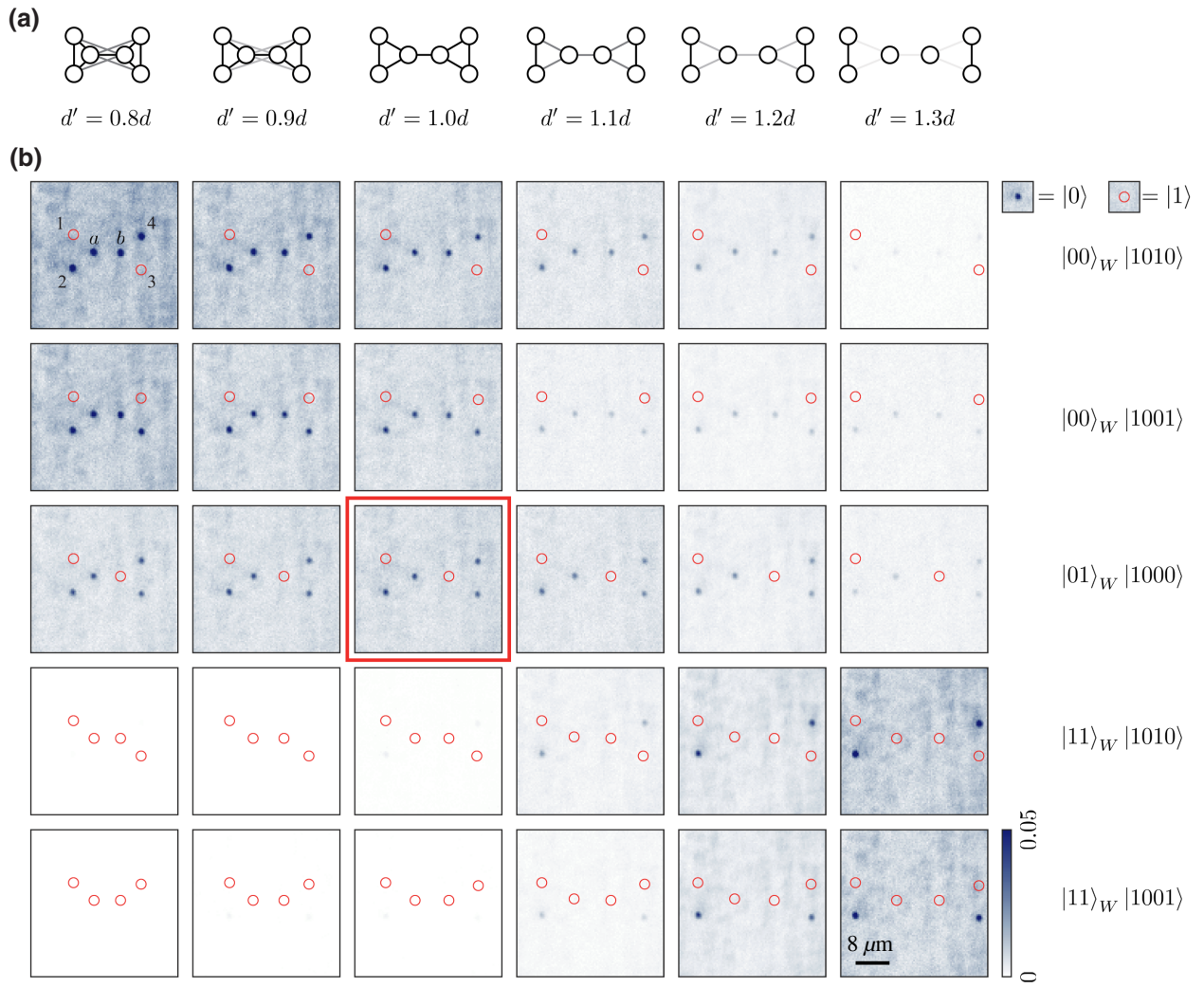


FIG. 3. The  $K'_4$ -like graphs of two types of edges. (a) Six different graphs are constructed with  $d'/d = 0.8, 0.9, 1.0, 1.1, 1.2$ , and  $1.3$  (from left to right), among which the  $d' = d = 0.76d_R$  graph corresponds to  $K'_4$ . (b) Fluorescence images of the atom arrays driven to  $H(\Omega_f = 0, \Delta_f = 2.0$  MHz,  $U = 3.9$  MHz) and sorted based on their spin configurations. Five characteristic spin configurations are shown (from top to bottom):  $|00\rangle_W|1010\rangle$ ,  $|00\rangle_W|1001\rangle$ ,  $|01\rangle_W|1000\rangle$ ,  $|11\rangle_W|1010\rangle$ , and  $|11\rangle_W|1001\rangle$ . The scale bar represents the relative probabilities of the configurations per graph. The numbers of collected events are 1057, 971, 927, 906, 2866, and 918 (from left to right), respectively, for the graphs.

numerical validations, for all Platonic graphs including the cube,  $Q'_3$ , and the octahedron,  $K'_{2,2,2}$ , in the following experiments.

The main results of the quantum simulation experiments of the Platonic graphs are summarized in Fig. 4. The atom arrays of the quantum-wired graphs,  $G' = K'_4$ ,  $Q'_3$ , and  $K'_{2,2,2}$ , are adiabatically driven from the PM<sub>↓</sub> phase to their MIS phases and their probabilities are plotted in Fig. 4(a)–4(c), respectively, for their spin configurations.

### A. Tetrahedron

In Fig. 4(a), we plot the experimental probability distribution,  $|\langle n | \text{Exp}(K'_4) \rangle|^2$ , where  $n$  enumerates the spin configuration of the  $K'_4$  atom array of the

four unwired- $K_4$  atoms and the two wire atoms in such a way that  $|n = 1\rangle = |00\rangle_W \otimes |0000\rangle$ ,  $|n = 2\rangle = |00\rangle_W \otimes |0001\rangle$ , ...,  $|n = 64\rangle = |11\rangle_W \otimes |1111\rangle$ . The shaded region in Fig. 4(a) corresponds to the spin configurations satisfying the AF condition of the quantum wire, where the high-population peaks in the AF region are  $|n = 21\rangle = |01\rangle_W|0100\rangle$ ,  $|n = 25\rangle = |01\rangle_W|1000\rangle$ ,  $|n = 34\rangle = |10\rangle_W|0001\rangle$ , and  $|n = 35\rangle = |10\rangle_W|0010\rangle$ , which agree well with the spin configurations of  $|M(K_4)\rangle$  in Eq. (2). In Fig. 4(d), we plot the probabilities (renormalized) in the second and third quadrants of Fig. 4(a). There are four dominant peaks of  $|n' = 5\rrangle = |01\rangle_W|0100\rangle$ ,  $|n' = 9\rangle = |01\rangle_W|1000\rangle$ ,  $|n' = 18\rangle = |10\rangle_W|0001\rangle$ , and  $|n' = 19\rangle = |10\rangle_W|0010\rangle$ . While, in an ideal case of experimental errors, these states

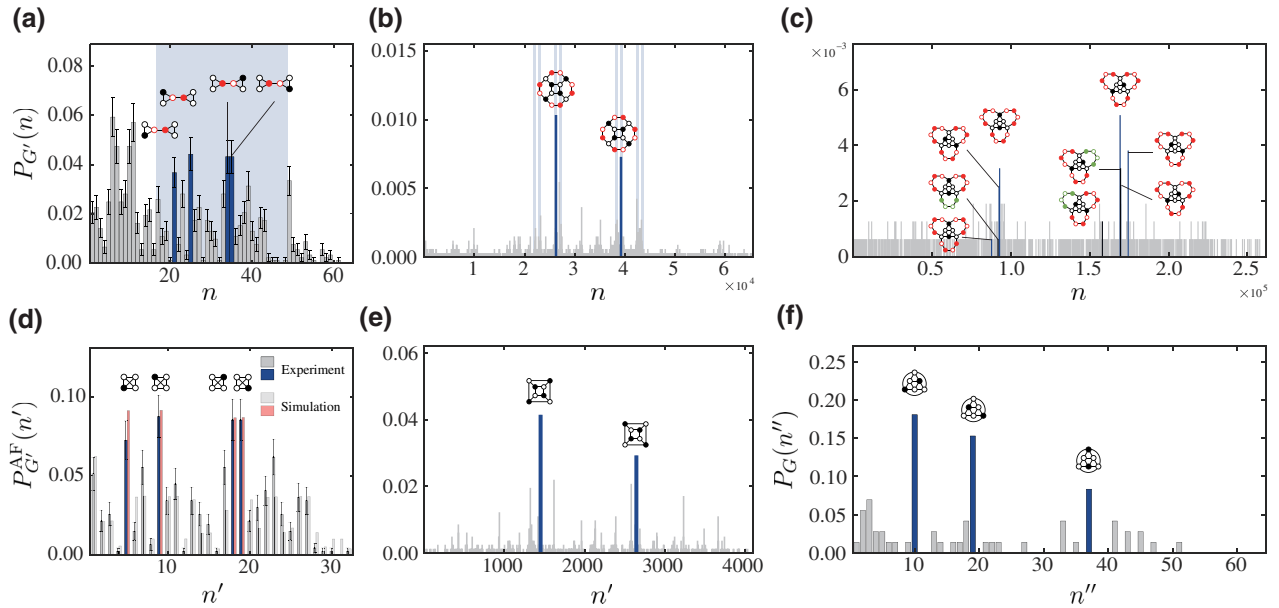


FIG. 4. (a)–(c) The experimental probability distributions,  $P_{G'}(n) = |\langle n | \text{Exp}(G') \rangle|^2$ , of the quantum-wired Platonic graphs  $G'$ 's driven to their MIS phases, where the index  $n = 1, \dots, 2^{|G'|}$  enumerates the spin configurations of (a)  $G' = K'_4$ , (b)  $Q'_3$ , and (c)  $K'_{2,2,2}$ . In (a)–(c), the numbers of collected experimental events are 927, 3292, and 1574, respectively. (d) The AF-conditional probability distributions  $P_{K'_4}^{\text{AF}}(n')$  (renormalized), which collects only the spin configurations satisfying the quantum-wire AF conditions, where the index  $n' = 1, \dots, 2^{|K_4|} \times 2$  counts the  $K_4$  spin states and the two quantum-wire states,  $|01\rangle_W$  and  $|10\rangle_W$ , compared with a numerical simulation of the evolved dynamics. (e) The AF-condition probabilities,  $P_{Q'_3}^{\text{AF}}(n')$  (renormalized), where  $n' = 1, \dots, 2^{|Q'_3|} \times 16$  counts the  $Q_3$  spin states and the 16 AF quantum wire states,  $\{|01\rangle, |10\rangle\}^{\otimes 4}$  of the four quantum wires  $W_1$ – $W_4$ . (f) The AF-condition probabilities  $P_{K'_{2,2,2}}^{\text{AF}}(n'')$  summed over the all AF quantum-wire spin states,  $\{|0101\rangle, |1010\rangle\}^{\otimes 3}$ , i.e.,  $P_{K'_{2,2,2}}(n'') = \sum_{\text{AF}} P_{K'_{2,2,2}}^{\text{AF}}(n'')$ , where  $n'' = 1, \dots, 2^{|K'_{2,2,2}|}$  counts the  $K_{2,2,2}$  spin states. In (d)–(f), there remain 469, 820, and 72 events, respectively.

are supposed to be of the same 25% populations, the experimentally observed populations are about 7%–9%. In order to take experimental errors into account, we numerically trace the quantum evolution of the  $K'_4$  atoms along the adiabatic control path introduced in Sec. IV using a Lindblad master equation [38] and considering laser phase noises and bit-flip detection errors [39,40]. The numerically obtained populations are about 10%, as shown in Fig. 4(d), which is consistent with the observed populations.

## B. Cube

The experimentally observed probability distribution,  $|\langle n | \text{Exp}(Q'_3) \rangle|^2$ , are plotted in Fig. 4(b), where the index  $n = 1, \dots, 2^{16}$  enumerates the spin configurations of the 16 atoms in  $Q'_3$ , among which eight are of the four quantum wires. In the MIS phase of the  $Q'_3$  graph, we expect that

$$\begin{aligned} |M(Q'_3)\rangle &= (|01\rangle_{W_1} |10\rangle_{W_2} |01\rangle_{W_3} |10\rangle_{W_4} |10101010\rangle \\ &\quad + |10\rangle_{W_1} |01\rangle_{W_2} |10\rangle_{W_3} |01\rangle_{W_4} |01010101\rangle) \\ &/\sqrt{2}, \end{aligned} \quad (7)$$

because the state of each wire-atom pair that couples a pair of  $Q_3$  atoms in  $|01\rangle$  ( $|10\rangle$ ) is determined to be  $|10\rangle_W$  ( $|01\rangle_W$ ). In Fig. 4(b), we observe two maximum-populated spin configurations,  $|n = 26\,283\rangle$  and  $|n = 39\,254\rangle$ , which agree well with the two spin configurations in  $|M(Q'_3)\rangle$  in Eq. (7). In Fig. 4(e), we plot, after normalization, the populations of only the spin configurations satisfying the AF condition, in which the eight quantum-wire atoms are represented in 16 base states from  $|01\rangle_{W_1} |01\rangle_{W_2} |01\rangle_{W_3} |01\rangle_{W_4}$  to  $|10\rangle_{W_1} |10\rangle_{W_2} |10\rangle_{W_3} |10\rangle_{W_4}$ . Then, the two dominant peaks are  $|n' = 1451\rangle = |01\rangle_{W_1} |10\rangle_{W_2} |01\rangle_{W_3} |10\rangle_{W_4} |10101010\rangle$  and  $|n' = 2646\rangle = |10\rangle_{W_1} |01\rangle_{W_2} |10\rangle_{W_3} |01\rangle_{W_4} |01010101\rangle$  as in Fig. 4(e), the results of which agree well with the two spin configurations in  $|M(Q'_3)\rangle$  in Eq. (5).

## C. Octahedron

In Fig. 4(c), we plot  $|\langle n | \text{Exp}(K'_{2,2,2}) \rangle|^2$ , the experimental probability distribution of  $K'_{2,2,2}$ , which has 12 quantum-wire atoms and six unwired- $K_{2,2,2}$  atoms. The MIS ground state of the  $K'_{2,2,2}$  is a little complicated. Among the three quantum wires, each of which has four wire atoms as in Fig. 1(c), two quantum wires—say,  $W_1$  and  $W_2$  for the case when atoms 3 and 6 are Rydberg atoms—must be in the

AF states  $|W_1\rangle = |1010\rangle$  and  $|W_2\rangle = |0101\rangle$  but then the other quantum wire,  $W_3$ , can be in either  $|1001\rangle$ ,  $|0101\rangle$  or

$|1010\rangle$ , which contribute the same energy. Therefore, the MIS ground state of  $K'_{2,2,2}$  is given by

$$\begin{aligned} |M(K'_{2,2,2})\rangle &= |1010\rangle_{W_1}|0101\rangle_{W_2}(a(|0101\rangle + |1010\rangle) + b|1001\rangle)_{W_3}|001001\rangle \\ &\quad + (a(|0101\rangle + |1010\rangle) + b|1001\rangle)_{W_1}|1010\rangle_{W_2}|0101\rangle_{W_3}|010010\rangle \\ &\quad + |0101\rangle_{W_1}(a(|0101\rangle + |1010\rangle) + b|1001\rangle)_{W_2}|1010\rangle_{W_3}|100100\rangle, \end{aligned} \quad (8)$$

where  $a = \sqrt{20/243}$  and  $b = \sqrt{41/243}$  are normalization factors. In the  $K'_{2,2,2}$  experimental results in Fig. 4(c), however, due to the limited statistics, it is unclear whether there are nine peaks as expected from Eq. (8). We first impose the AF quantum-wire condition and then add their probabilities (i.e., there are eight quantum-wire configurations from  $|0101\rangle_{W_1}|0101\rangle_{W_2}|0101\rangle_{W_3}$  to  $|1010\rangle_{W_1}|1010\rangle_{W_2}|1010\rangle_{W_3}$ ), for each unwired- $K_{2,2,2}$  spin configuration enumerated with  $n'' = 1, \dots, 2^6$ . In Fig. 4(f), we observe three clear peaks,  $|n'' = 10\rangle$ ,  $|n'' = 19\rangle$ , and  $|n'' = 37\rangle$ , which correspond to the spin configurations,  $|001001\rangle$ ,  $|010010\rangle$ , and  $|100100\rangle$ , respectively, of the MIS phase of  $K_{2,2,2}$ , agreeing well with  $|M(K_{2,2,2})\rangle$ .

## VI. DISCUSSION AND OUTLOOK

We now turn our attention to the scaling issue involved with the current method of graph transformation from 3D surfaces to two-dimensional (2D) planes. Our experiment presents the transformation of the tetrahedron graph  $K_4$  of  $N = 4$  atoms to the quantum-wired graph  $K'$  of total  $N' = 6$  atoms, the cube graph  $Q_3$  of  $N = 8$  to  $Q'_3$  of  $N' = 16$ , and the octahedron graph  $K_{2,2,2}$  of  $N = 6$  to  $K'_{2,2,2}$  of  $N' = 18$ . In Fig. 5, we plot  $N$  versus  $N'$  for these three Platonic graphs and we also plot other examples of the remaining Platonic graphs, the icosahedron and dodecahedron graphs, and two fullerene graphs,  $C_{24}$  and  $C_{60}$ . We observe a linear relationship between  $N$  and  $N'$ , the scaling of which can be understood as follows. When we move the vertices from the sphere of radius  $R$  to the square plane of length  $L$ , we expect  $L \sim R$ , because the distances of the vertices along a chosen circumference of the sphere can optionally be kept unchanged. The number  $N$  of a graph  $G$  scales with  $N \sim R^2/d_R^2$  and  $N'$  of  $G'$  scales with  $N' \sim L^2/d_R^2$ . So, the quantum-wired graph  $G'$  can be constructed with  $N' \sim N$  to transform  $G$  from 3D to 2D.

While the number of atoms required for the 3D-to-2D transformation is scaled favorably, the actual  $N'$  in our quantum-wired graph experiments is limited by, for example, the rearrangement probability and the bit-flip errors.

When  $N'$  atoms are to be rearranged into chosen positions, the rearrangement probability of  $N'$  atoms is given by  $P_r = p^{N'}$ , where  $p = \exp(-t/t_0) = 0.97$  is the vacuum-limited single-atom survival probability for an average trap lifetime of  $t_0 = 16$  s and a rearrangement time of  $t = 0.5$  s, which gives  $N' < 80$  for  $P_r > 0.01$ . The bit-flip errors  $P_{0 \rightarrow 1}$  and  $P_{1 \rightarrow 0}$ , due to imperfections of the state preparation and measurement, result in statistical ambiguities of the ground-state probability,  $P_g' \sim (1 - P_{0 \rightarrow 1})^{N'/2}(1 - P_{1 \rightarrow 0})^{N'/2}P_g$ , and the probabilities of other states,  $P_{\text{others}} \sim P_{0 \rightarrow 1}(1 - P_{0 \rightarrow 1})^{N'/2-1}(1 - P_{1 \rightarrow 0})^{N'/2}P_g$ , where  $P_g$  is a unity ground-state probability assuming an ideal situa-

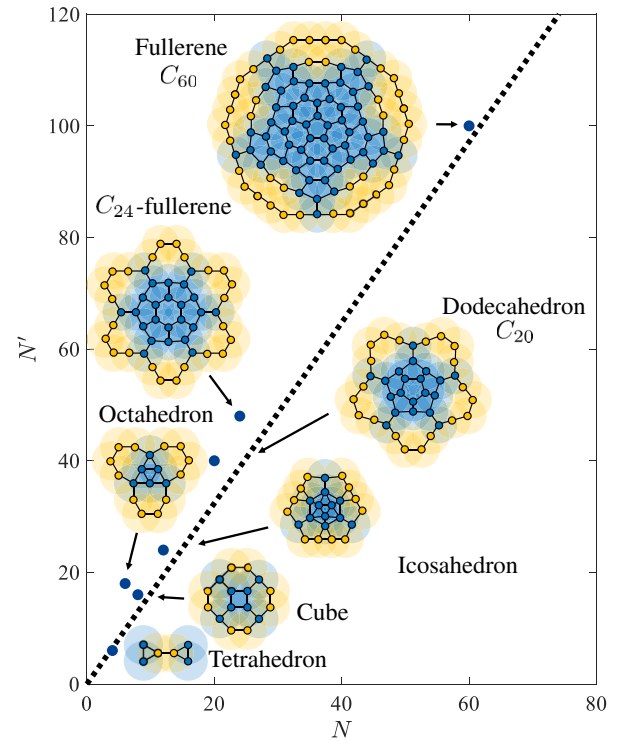


FIG. 5. The atom-number scaling of  $N'$ , of a quantum-wire graph  $G'$ , versus  $N$ , of a target graph  $G$ .

tion with perfect adiabatic control. A criterion of sufficient measurements where the statistical uncertainties of  $P'_g$  and  $P_{\text{others}}$  do not overlap, i.e.,  $|P'_g - P_{\text{others}}| \sim \sqrt{P'_g(1 - P'_g)/M + \sqrt{P_{\text{others}}(1 - P_{\text{others}})/M}}$ , where  $M$  is the number of measurements, demands about  $M/P_r = 100$  repeated experiments, which takes approximately 2 min for  $N' = 25$  and about  $M/P_r = 2 \times 10^5$  experiments, or approximately 3 days, for  $N' = 80$ . The scale of the expected fidelity can also be simply estimated, being proportional to the fraction of the number of antiferromagnetic configurations in the full ground states, which is approximately  $O(1/N)$ , under the assumption that the quantum wires operate independently. Both of the considered experimental limitations can be improved by using the state-of-the-art Rydberg-atom technologies. One approach to increase the rearrangement probability is to use a cryogenic environment of trapped atoms [41], in which the trap lifetime is measured to be  $t_0 = 6 \times 10^3$  s. It is expected that the single-atom survival probability  $p = 0.9999$  in the cryogenic setup can achieve  $N' > 1000$  for  $P_r = 0.9$ . The bit-flip errors are significantly reduced with alkaline-earth atomic systems [42], where  $P_{0 \rightarrow 1}$  and  $P_{1 \rightarrow 0}$  are less than 0.01. We expect that such improved bit-flip errors can reduce the required number of experimental repetitions, enabling us to access  $N' \sim 1000$  atoms, which only takes  $M/P_r = 3 \times 10^4$  measurements or about 8 h.

In summary, we perform Rydberg-atom experiments to find the MISs of three Platonic graphs: the tetrahedron, cube, and octahedron graphs. We experimentally obtain their many-body ground states in antiferromagnetic phases, which are the MISs of the given graphs. While the Platonic graphs are 3D structures, we use Rydberg-atom quantum wires to transform them into 2D structures, in which the quantum wires adjust the coupling strengths of the stretched edges to be the same as those of the unstretched edges. With the 2D quantum-wired graphs, we control the atom-array Hamiltonians adiabatically from their paramagnetic phase to the AF phases and obtain their many-body AF ground-state spin configurations. The results are in good agreement with the symmetry analysis and numerical simulations. The topology-preserving 3D-to-2D transformation technique of Ising spin networks is a versatile alternative to the direct 3D-atom arrangement and detection methods [12,43], which are technically nascent for large scales. It is estimated that this approach of using quantum wires to transform 3D planar-graph structures could achieve, in conjunction with alkaline-earth atom technologies in cryogenic environments, more than 1000-atom quantum simulations. We hope that this technique can be applied to access not only the MIS problems but also other nondeterministic polynomial problems that can be mapped to Ising models [44].

The experimental data set is archived in Ref. [45] for further analysis.

## ACKNOWLEDGMENTS

This research was supported by the Samsung Science and Technology Foundation (Grant No. SSTF-BA 1301-52).

- [1] I. M. Georgescu, S. Ashhab, and F. Nori, Quantum simulation, *Rev. Mod. Phys.* **86**, 153 (2014).
- [2] C. Monroe, W. C. Campbell, L.-M. Duan, Z.-X. Gong, A. V. Gorshkov, P. W. Hess, R. Islam, K. Kim, N. M. Linke, G. Pagano, P. Richerme, C. Senko, and N. Y. Yao, Programmable quantum simulations of spin systems with trapped ions, *Rev. Mod. Phys.* **93**, 025001 (2021).
- [3] S. A. Wilkinson and M. J. Hartmann, Superconducting quantum many-body circuits for quantum simulation and computing, *Appl. Phys. Lett.* **116**, 230501 (2020).
- [4] I. Bloch, J. Dalibard, and S. Nascimbene, Quantum simulations with ultracold quantum gases, *Nat. Phys.* **8**, 267 (2012).
- [5] J. Du, N. Xu, X. Peng, P. Wang, S. Wu, and D. Lu, NMR Implementation of a Molecular Hydrogen Quantum Simulation with Adiabatic State Preparation, *Phys. Rev. Lett.* **104**, 030502 (2010).
- [6] M. Saffman, T. G. Walker, and K. Mølmer, Quantum information with Rydberg atoms, *Rev. Mod. Phys.* **82**, 2313 (2010).
- [7] M. Saffman, Quantum computing with atomic qubits and Rydberg interactions: Progress and challenges, *J. Phys. B: At. Mol. Opt. Phys.* **49**, 202001 (2016).
- [8] A. Browaeys, D. Barredo, and T. Lahaye, Experimental investigations of dipole-dipole interactions between a few Rydberg atoms, *J. Phys. B: At. Mol. Opt. Phys.* **49**, 152001 (2016).
- [9] A. Browaeys and T. Lahaye, Many-body physics with individually controlled Rydberg atoms, *Nat. Phys.* **16**, 132 (2020).
- [10] M. Morgado and S. Whitlock, Quantum simulation and computing with Rydberg-interacting qubits, *AVS Quantum Sci.* **3**, 023501 (2021).
- [11] H. Labuhn, D. Barredo, S. Ravets, S. de Léséleuc, T. Macrì, T. Lahaye, and A. Browaeys, Tunable two-dimensional arrays of single Rydberg atoms for realizing quantum Ising models, *Nature* **534**, 667 (2016).
- [12] M. Kim, Y. Song, J. Kim, and J. Ahn, Quantum-Ising Hamiltonian Programming In Trio, Quartet, and Sextet Qubit Systems, *PRX Quantum* **1**, 020323 (2020).
- [13] D. Barredo, H. Labuhn, S. Ravets, T. Lahaye, A. Browaeys, and C. S. Adams, Coherent Excitation Transfer in a Spin Chain of Three Rydberg Atoms, *Phys. Rev. Lett.* **114**, 113002 (2015).
- [14] S. de Léséleuc, D. Barredo, V. Lienhard, A. Browaeys, and T. Lahaye, Optical Control of the Resonant Dipole-Dipole Interaction between Rydberg Atoms, *Phys. Rev. Lett.* **119**, 053202 (2017).
- [15] P. Scholl, H. J. Williams, G. Bornet, F. Wallner, D. Barredo, T. Lahaye, A. Browaeys, L. Henriet, A. Signoles, C. Hainaut, T. Franz, S. Geier, A. Tebben, A. Salzinger, G. Zürn, and M. Weidemüller, Microwave-engineering of

- programmable XXZ Hamiltonians in arrays of Rydberg atoms, [ArXiv:2107.14459](#) (2021).
- [16] H. Kim, W. Lee, H.-G. Lee, H. Jo, Y. Song, and J. Ahn, *In situ* single-atom array synthesis by dynamic holographic optical tweezers, *Nat. Commun.* **7**, 13317 (2016).
- [17] D. Barredo, S. de Léséleuc, V. Lienhard, T. Lahaye, and A. Browaeys, An atom-by-atom assembler of defect-free arbitrary 2D atomic arrays, *Science* **354**, 1021 (2016).
- [18] M. Endres, H. Bernien, A. Keesling, H. Levine, E. R. Anschuetz, A. Krajenbrink, and M. D. Lukin, Atom-by-atom assembly of defect-free one-dimensional cold atom arrays, *Science* **354**, 1024 (2016).
- [19] A. Omran, H. Levine, A. Keesling, G. Semeghini, T. T. Wang, S. Ebadi, H. Bernien, A. S. Zibrov, H. Pichler, S. Choi, J. Cui, M. Rossignolo, P. Rembold, S. Montangero, T. Calarco, M. Endres, M. Greiner, V. Vuletić, and M. D. Lukin, Generation and manipulation of Schrödinger cat states in Rydberg atom arrays, *Science* **365**, 570 (2019).
- [20] P. Schauß, J. Zeiher, T. Fukuhara, S. Hild, M. Cheneau, T. Macri, T. Pohl, I. Bloch, and C. Gross, Crystallization in Ising quantum magnets, *Science* **347**, 1455 (2015).
- [21] H. Bernien, S. Schwartz, A. Keesling, H. Levine, A. Omran, H. Pichler, S. Choi, A. S. Zibrov, M. Endres, M. Greiner, V. Vuletić, and M. D. Lukin, Probing many-body dynamics on a 51-atom quantum simulator, *Nature* **551**, 579 (2017).
- [22] V. Lienhard, S. de Léséleuc, D. Barredo, T. Lahaye, A. Browaeys, M. Schuler, L.-P. Henry, and A. M. Läuchli, Observing the space- and time-dependent growth of correlations in dynamically tuned synthetic Ising models with antiferromagnetic interactions, *Phys. Rev. X* **8**, 021070 (2018).
- [23] A. Keesling, A. Omran, H. Levine, H. Bernien, H. Pichler, S. Choi, R. Samajdar, S. Schwartz, P. Silvi, S. Sachdev, P. Zoller, M. Endres, M. Greiner, V. Vuletić, and M. D. Lukin, Quantum Kibble-Zurek mechanism and critical dynamics on a programmable Rydberg simulator, *Nature* **568**, 207 (2019).
- [24] D. Bluvstein, A. Omran, H. Levine, A. Keesling, G. Semeghini, S. Ebadi, T. T. Wang, A. A. Michailidis, N. Maskara, W. W. Ho, S. Choi, M. Serbyn, M. Greiner, V. Vuletic, and M. D. Lukin, Controlling quantum many-body dynamics in driven Rydberg atom arrays, *Science* **371**, 6536 (2021).
- [25] G. Semeghini, H. Levine, A. Keesling, S. Ebadi, T. T. Wang, D. Bluvstein, R. Verresen, H. Pichler, M. Kalinowski, R. Samajdar, A. Omran, S. Sachdev, A. Vishwanath, M. Greiner, V. Vuletić, and M. D. Lukin, Probing topological spin liquids on a programmable quantum simulator, *Science* **374**, 1242 (2021).
- [26] W. Lee, H. Kim, and J. Ahn, Three-dimensional rearrangement of single atoms using actively controlled optical microtraps, *Opt. Express* **24**, 9816 (2016).
- [27] D. Barredo, V. Lienhard, S. Léséleuc, T. Lahaye, and A. Browaeys, Synthetic three-dimensional atomic structures assembled atom by atom, *Nature* **561**, 79 (2018).
- [28] Y. Song, M. Kim, H. Hwang, W. Lee, and J. Ahn, Quantum simulation of Cayley-tree Ising Hamiltonians with three-dimensional Rydberg atoms, *Phys. Rev. Res.* **3**, 013286 (2021).
- [29] P. Scholl, M. Schuler, H. J. Williams, A. A. Eberharter, D. Barredo, K-N. Schymik, V. Lienhard, L-P. Henry, T. C. Lang, T. Lahaye, A. M. Läuchli, and A. Browaeys, Quantum simulation of 2D antiferromagnets with hundreds of Rydberg atoms, *Nature* **595**, 233 (2021).
- [30] S. Ebadi, T. T. Wang, H. Levine, A. Keesling, G. Semeghini, A. Omran, D. Bluvstein, R. Samajdar, H. Pichler, W. W. Ho, S. Choi, S. Sachdev, M. Greiner, V. Vuletić, and M. D. Lukin, Quantum phases of matter on a 256-atom programmable quantum simulator, *Nature* **595**, 227 (2021).
- [31] H. Pichler, S.-T. Wang, L. Zhou, S. Choi, and M. D. Lukin, Quantum optimization for maximum independent set using Rydberg atom arrays, [ArXiv:1808.10816](#) (2018).
- [32] H. Pichler, S.-T. Wang, L. Zhou, S. Choi, and M. D. Lukin, Computational complexity of the Rydberg blockade in two dimensions, [ArXiv:1809.04954](#) (2018).
- [33] M. Kim, K. Kim, J. Hwang, E-G. Moon, and J. Ahn, Rydberg quantum wires for maximum independent set problems, *Nature Phys.*, <https://www.nature.com/articles/s41567-022-01629-5>.
- [34] S. Ebadi, *et al.*, Quantum optimization of maximum independent set using Rydberg atom arrays, [ArXiv:2202.09372](#).
- [35] T. Albash and D. A. Lidar, Adiabatic quantum computation, *Rev. Mod. Phys.* **90**, 015002 (2018).
- [36] X. Qiu, P. Zoller, and X. Li, Programmable Quantum Annealing Architectures with Ising Quantum Wires, *PRX Quantum* **1**, 020311 (2020).
- [37] J. Zeiher, P. Schauß, S. Hild, T. Macri, I. Bloch, and C. Gross, Microscopic characterization of scalable coherent Rydberg superatoms, *Phys. Rev. X* **5**, 031015 (2015).
- [38] G. Lindblad, On the generators of quantum dynamical semigroups, *Commun. Math. Phys.* **48**, 119 (1976).
- [39] S. de Léséleuc, D. Barredo, V. Lienhard, A. Browaeys, and T. Lahaye, Analysis of imperfections in the coherent optical excitation of single atoms to Rydberg states, *Phys. Rev. A* **97**, 053803 (2018).
- [40] W. Lee, M. Kim, H. Jo, Y. Song, and J. Ahn, Coherent and dissipative dynamics of entangled few-body systems of Rydberg atoms, *Phys. Rev. A* **99**, 043404 (2019).
- [41] K.-N. Schymik, S. Pancaldi, F. Nogrette, D. Barredo, J. Paris, A. Browaeys, and T. Lahaye, Single Atoms with 6000-Second Trapping Lifetimes in Optical-Tweezer Arrays at Cryogenic Temperatures, *Phys. Rev. Appl.* **16**, 034013 (2021).
- [42] I. S. Madjarov, J. P. Covey, A. L. Shaw, J. Choi, A. Kale, A. Cooper, H. Pichler, V. Schkolnik, J. R. Williams, and M. Endres, High-fidelity entanglement and detection of alkaline-earth Rydberg atoms, *Nat. Phys.* **16**, 857 (2020).
- [43] H. Sun, Y. Song, A. Byun, H. Jeong, and J. Ahn, Imaging three-dimensional single-atom arrays all at once, *Opt. Express* **29**, 4082 (2021).
- [44] A. Lucas, Ising formulations of many NP problems, *Front. Phys.* **2**, 5 (2014).
- [45] A. Byun, M. Kim, and J. Ahn, The digitized datasets for the quantum-wired tetrahedron, cube, and octahedron graphs, (2022).